ADVANCED ENERGY MATERIALS

# Supporting Information

for *Adv. Energy Mater.*, DOI: 10.1002/aenm.201901377

# High Thermoelectric Performance in PbSe–$NaSbSe_2$ Alloys from Valence Band Convergence and Low Thermal Conductivity

*Tyler J. Slade, Trevor P. Bailey, Jann A. Grovogui, Xia Hua, Xiaomi Zhang, Jimmy Jiahong Kuo, Ido Hadar, G. Jeffrey Snyder, Chris Wolverton, Vinayak P. Dravid, Ctirad Uher, and Mercouri G. Kanatzidis**

WILEY-VCH



# Supporting Information

# High Thermoelectric Performance in PbSe–$NaSbSe_2$ Alloys from Valence Band Convergence and Low Thermal Conductivity

*Tyler J. Slade,[1] Trevor P. Bailey,[2] Jann A. Grovogui,[3] Xia Hua,[3] Xiaomi Zhang,[3] Jimmy Jiahong Kuo,[3] Ido Hadar,[1] G. Jeffrey Snyder,[3] Vinayak P. Dravid[3], Chris Wolverton[3], Ctirad Uher[2], Mercouri G. Kanatzidis[1,*]*

[1]Department of Chemistry, Northwestern University, Evanston, Illinois 60208, USA.
[2]Department of Physics, University of Michigan, Ann Arbor, Michigan 48109, USA.
[3]Department of Materials Science and Engineering, Northwestern University, Evanston, Illinois 60208, USA.

*Corresponding author: M. G. Kanatzidis (m-kanatzidis@northwestern.edu).*

## Additional details on experiments and calculations:

**Powder X-ray diffraction***:* Powder X-ray diffraction (PXRD) patterns were measured on a Rigaku Miniflex 600 instrument with Cu Kα radiation (λ = 1.5406 Å) at 40 kV and 15 mA and with a $K_\beta$ filter. Lattice parameters were refined using the Rietveld method in GSAS-II software.

**Fourier transformed infrared spectroscopy (FT-IR):** Optical band gaps were determined by diffuse reflectance measurements performed with a Nicolet 6700 FT-IR spectrometer. Samples consisted of powders prepared by finely grinding the SPSed $NaPb_mSbSe_{m+2}$ in a mortar and pestle. The reflectance data was converted to absorption with the Kubelka–Munk equation $\alpha/S = (1-R)^2/2R$ where $R$ is the reflectance, and $\alpha$ and $S$ are the absorption and scattering coefficients, respectively. The band gaps were estimated by extrapolating the absorption edges of each spectra.

**Calculation of the Lorenz number and estimation of the lattice thermal conductivity:** For the nominally undoped $NaPb_mSbSe_{m+2}$ compounds, we calculated the Lorenz number using the following equation for nondegenerate semiconductors:[1]

$$L = \left(r + {}^5/_2\right)\left(\frac{k_B}{e}\right)^2$$

(S1)

Where $k_B$ is the Boltzmann constant, $e$ is the electron charge, and $r$ gives the energy dependence of the relaxation time. Here, we used $r$ = -1/2 characteristic of acoustic phonon scattering, which yields $L$ = 1.485x10$^{-8}$ V$^2$·K$^{-2}$. While the acoustic phonon scattering assumption is not valid in our compounds under 500 K where grain boundary scattering dominates the transport, we expect this to ultimate contribute negligible errors to the estimation of the lattice thermal conductivities in the undoped samples because the electrical conductivities are all very low (under 80 S·cm$^{-3}$).

In the case of the doped samples: $Na_{1+x}Pb_{10-x}SbSe_{m+2}$ and $Na_{1+x}Pb_{10}Sb_{1-x}Se_{m+2}$, we estimated the temperature dependence of $L$ by fitting the reduced chemical potential $\eta$ to the measured Seebeck coefficients as shown below:[2]

$$S = \frac{k_B}{e}\left(\frac{2F_1(\eta)}{F_0(\eta)} - \eta\right)$$

(S2)

where $F_j(\eta)$ are the Fermi-Dirac integrals defined as follows:

$$F_j(\eta) = \int_0^\infty \frac{\varepsilon^j d\varepsilon}{1+e^{(\varepsilon-\eta)}}$$

(S3)

and $\varepsilon$ is the reduced carrier energy. The values of η that fit the temperature-dependent Seebeck coefficients were then used to calculate $L$ through

$$L = \left(\frac{k}{e}\right)^2 \left(\frac{3F_0(\eta)F_2(\eta)-4F_1(\eta)^2}{F_0(\eta)^2}\right)$$

(S4)

This fitting process assumes a single parabolic band dominated by acoustic phonon scattering and an energy-independent scattering time. Calculated values of $L$ are shown in Figure S2 and the corresponding electronic thermal conductivities in Figure S3.

Once we determined the temperature depend values of $L$, the electronic ($\kappa_{elec}$) and lattice ($\kappa_{lat}$) thermal conductivities were calculated using the following:

$$\kappa_{elec} = \sigma L T$$

(S5)

$$\kappa_{lat} = \kappa_{tot} - \kappa_{elec}$$

(S6)

Where $\sigma$ is the electrical conductivity, $T$ is the absolute temperature and $\kappa_{tot}$ is the total thermal conductivity.

**Impact of the grain boundary charge carrier scattering on the estimated lattice thermal conductivity:** As alluded to in the main text, the process described above will impede reliable estimation of the lattice thermal conductivity. This occurs because most of the heat transported by charge carriers will come from the electrical conduction in the bulk grains, where $\sigma$ is presumably much higher than our measured values. Our measured $\sigma$ are lower than the true bulk values because the electrical conductivities are dominated by the GBs below 500 K. As a consequence, the values of $\sigma$ reported in the main text below 500 K reflect only the electrical conduction at the GBs, leaving the bulk electrical conductivity unknown. Therefore, our estimations of $\kappa_{elec}$ also are reflective only of the GBs and are severely underestimated when the GB charge carrier scattering is strong, leading to potentially severe overestimation of $\kappa_{lat}$. Indeed, comparing the $\kappa_{lat}$ presented in Figure 4b with the corresponding electrical conductivities plotted in Figure 3a, we indeed see that the compounds with strongest GB scattering (x = 0.05–0.15) appear to have the highest estimated lattice thermal conductivities under 500 K, exactly as anticipated from the above analysis.

**Pisarenko plots:** To compliment the predictions of band convergence indicated by the DFT calculated band structures, we compared theoretical plots of carrier density (*n*) vs. Seebeck coefficient generated using a single Kane band (SKB) model and a two-band model. The SKB Pisarenko plots utilized following equations,[1, 3, 4]

$$n = \frac{(m^*_{DOS} k_B T)^{3/2}}{2\pi^2 \hbar^3} \; {}^0F_0^{3/2}$$

(S7)

where $m^*_{DOS}$ is the density of states effective mass and ħ is the Planck constant. The Hall coefficient $R_H$ and carrier density are related by:

$$R_H = A/en$$

(S8)

and *A* is the Hall factor given as:

$$A = \frac{3K(K+2)}{(2K+1)^2} \frac{{}^0F_{-4}^{1/2} \cdot {}^0F_0^{3/2}}{({}^0F_{-2}^1)^2}$$

(S9)

Where *K* parameterizes the anisotropy of the band structure and is equal to 1.75 for PbSe.[4] The Seebeck coefficients are calculated as follows:

$$S = \frac{k_B}{e}\left(\frac{{}^1F_{-2}^1}{{}^0F_{-2}^1} - \eta\right)$$

(S10)

Where $\eta$ is the reduced chemical potential. The functions ${}^nF_k^m$ are of the following form,

$${}^nF_k^m = \int_0^\infty \left(\frac{-df}{d\varepsilon}\right) \varepsilon^n (\varepsilon + \alpha\varepsilon^2)^m [(1+\alpha\varepsilon)^2 + 2]^{k/2} d\varepsilon$$

(S11)

with $\alpha = \frac{k_b T}{E_g}$ and $E_g$ is the band gap. For the SKB Pisarenko plot calculations, we kept all of the above variables constant and varied the band effective mass to achieve the best fit to the experimental data. The band effective mass is related to the density of states mass through the band degeneracy $N_v$:

$$m^*_{DOS} = N_v^{2/3} m^*_b$$

(S12)

For the two-band model we utilized the relationships presented by Chasapis *et al*. in their work on Na doped PbSe.[5] Here, the thermoelectric properties of the *L*-band were calculated using the equations shown above for a single Kane type band. The *Σ*-band uses the

same equations but is considered parabolic by setting $\alpha = 0$ and $K = 1$. The parameters considered for the temperature dependent bands are shown below.

$$E_g = 0.25 + 0.0004 \cdot T \quad \text{(S13)}$$

$$\Delta E_{L-\Sigma} = 0.22 - 0.00022 \cdot T \quad \text{(S14)}$$

$$m_L^* = 0.14\ m_e \quad \text{(S15)}$$

$$m_\Sigma^* = 0.475\ m_e \quad \text{(S16)}$$

$$\eta_\Sigma = \eta_L - \Delta E_{L-\Sigma}/k_B T \quad \text{(S17)}$$

Where $\Delta E_{L-\Sigma}$ is the energy difference between the two bands and $m_L^*$ and $m_\Sigma^*$ are respectively the band effective mass of the $L$- and $\Sigma$-bands, and $\eta_\Sigma$ is the chemical potential of the $\Sigma$-band. The valley degeneracy of each band is 4 ($L$-band) and 12 ($\Sigma$-band). The temperature dependence of the $L$-band was assumed to follow the relationship $dln(m_b^*)/dln(T) = 0.5$ found by Wang et al.[4] Using the above parameters for each band, the carrier densities and Seebeck coefficients were calculated in the two-band model as follows:

$$n_H = n_L + n_\Sigma \quad \text{(S18)}$$

$$S = \frac{S_L\sigma_L + S_\Sigma\sigma_\Sigma}{\sigma_L + \sigma_\Sigma} \quad \text{(S19)}$$

**Debye-Callaway model for theoretical lattice thermal conductivity:** To gain insight into the origins of the low thermal conductivity measured in $NaPb_mSbSe_{m+2}$, we calculated theoretical values of $\kappa_{lat}$ based on a simplified Debye-Callway model.[6-8] Here, we only considered phonon-phonon scattering (Umklapp and Normal processes) and point defect phonon scattering processes. The lattice thermal conductivity is given as follows:

$$\kappa_{lat} = \frac{k_B}{2\pi^2 v}\left(\frac{k_B T}{\hbar}\right)^3 \int_0^{\theta_D/T} \tau_c(x) \frac{x^4 e^x}{(e^x-1)^2} dx$$

(S20)

where $x = \hbar\omega/k_B T$, $\omega$ is the phonon frequency, $\theta_D$ is the Debye temperature, $\tau_c$ is the combined phonon relaxation time, and $v$ is the phonon group velocity (equal to the average speed of sound in our polycrystalline samples). The combined relaxation time was found by summing the contributions from the various phonon scattering processes considered in our model.

$$\tau_c^{-1} = \tau_U^{-1} + \tau_N^{-1} + \tau_{PD}^{-1}$$

(S21)

The above correspond to the relaxation times for Umklapp, normal, and point defect phonon scattering respectively. In principle, many more mechanisms may contribute to phonon scattering such as grain boundaries, precipitates, phase boundaries, electron phonon interaction, etc.; however, we found that our simplified model matches experimental the data well near room temperature, suggesting that point defect phonon scattering is the primary origin of the low thermal conductivity.

The relaxation times for Umklapp and Normal processes are given in the following equations:

$$\tau_U^{-1} = \frac{\hbar\gamma^2}{M v^2 \theta_D}\omega^2 T \exp\left(\frac{-\theta_D}{3T}\right)$$

(S22)

$$\tau_N^{-1} = \beta\tau_U^{-1}$$

(S23)

Where $\gamma$ is the Gruneisen parameter, $M$ is the average mass of an atom in the crystal, and $\beta$ is a fitting constant used to determine the ratio of Umklapp to normal processes. $\beta$ was determined by fitting the calculated values of $\kappa_{lat}$ for experimental data to that of pure PbSe.

Lastly the relations for the point defect phonon scattering in a solid solution are shown below:

$$\tau_{PD}^{-1} = \frac{\omega^4 V}{4\pi v^3}\Gamma$$

(S24)

$$\Gamma = \Gamma_M + \Gamma_S$$

(S25)

where $V$ is the average volume of an atom in the crystal, and $\Gamma$ is the disorder scaling parameter which characterizes the phonon scattering from mass and strain field fluctuations between the host lattice and alloying atoms.

$$\Gamma_M = \frac{\sum_{i=1}^{n} c_i \left(\frac{<M_i>}{M^*}\right)^2 f_i^1 f_i^2 \left(\frac{M_i^1 - M_i^2}{<M_i>}\right)^2}{\sum_{i=1}^{n} c_i}$$

(S26)

$$\Gamma_S = \frac{\sum_{i=1}^{n} c_i \left(\frac{<M_i>}{M^*}\right)^2 f_i^1 f_i^2 \varepsilon \left(\frac{r_i^1 - r_i^2}{<r_i>}\right)^2}{\sum_{i=1}^{n} c_i}$$

(S27)

Where $c_i$ is the degeneracy (here $c_i$ = 2), $f_i^k$ is the fractional occupation of atom $k$ (Pb, Sb, Na), $< M_i >$ and $< r_i >$ are the average mass and radius of the $i$th sublattice ($< M_i > = \sum_k f_i^k M_i^k$ and $< r_i > = \sum_k f_i^k r_i^k$), and $M^*$ is the average atomic mass of the compound ($M^* = \frac{1}{2}\sum_i < M_i >$). $\varepsilon$ is a phenomenological parameter related to the lattice anharmonicity which was found by fitting the experimental data. Here, we found $\varepsilon$ = 90 to give a satisfactory fit, which is in reasonable agreement with previous studies on PbTe, which reported $\varepsilon$ = 110.[7, 8] The parameters used in the Debye-Callaway calculations are outlined below in Table S2.

**Table S1.** Constants and parameters used in the Debye-Callaway lattice thermal conductivity calculations for $NaPb_mSbSe_{m+2}$. The values of $v$, $\gamma$, $\theta_D$, and the radii were obtained from references 7 and 8.

| Parameters | Value |
|---|---|
| $\boldsymbol{v}$ | 1926.3 m·s$^{-1}$ |
| $\boldsymbol{\theta_D}$ | 125 K |
| $\gamma$ | 1.65 |
| $\boldsymbol{M_{Pb}}$ | 207.2 g·mol$^{-1}$ |
| $\boldsymbol{M_{Se}}$ | 78.96 g·mol$^{-1}$ |
| $\boldsymbol{M_{Na}}$ | 22.989 g·mol$^{-1}$ |
| $\boldsymbol{M_{Sb}}$ | 121.76 g·mol$^{-1}$ |
| $\boldsymbol{r_{Pb}}$ | 175 pm |
| $\boldsymbol{r_{Se}}$ | 115 pm |
| $\boldsymbol{r_{Na}}$ | 186 pm |
| $\boldsymbol{r_{Sb}}$ | 136 pm |
| $\beta$ (fit) | 3.8 |
| $\boldsymbol{\varepsilon}$ (fit) | 90 |

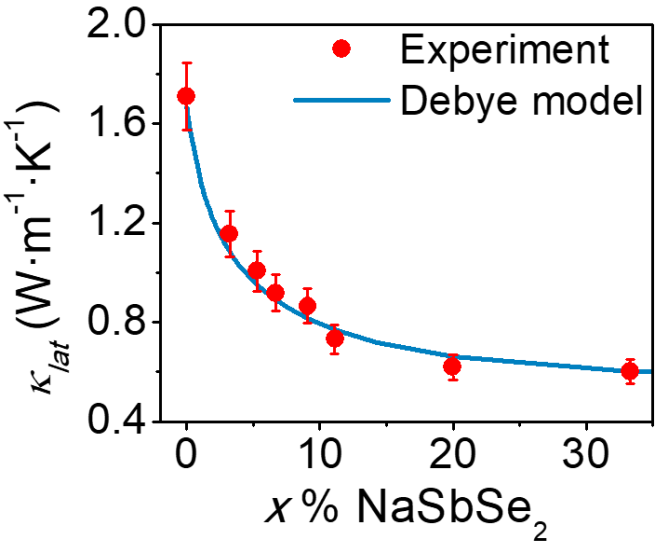


**Figure S1.** Experimentally determined lattice thermal conductivity for $NaPb_mSbSe_{m+2}$ for m = 2–30 and PbSe, plotted as % $NaSbSe_2$ in PbSe, compared with the theoretical curve generated from the simplified Debye-Callaway model. The experimental data is shown with 8% error bars.

**Average *ZT* calculations:** To estimate the theoretical efficiency of our $NaPb_mSbSe_{m+2}$ in a thermoelectric module, we utilized the procedure outlined by Snyder et al.[9] to estimate the average *ZT* ($ZT_{avg}$, often also found in other publications denoted as $ZT_{dev}$ or $ZT_{eng}$ ) considering cold and hot side temperatures of 400 and 873 K respectively. 400 K was chosen as the cold side temperature (instead of room temperature) because in realistic applications, energy is required to maintain the cold side at 300 K. This lowers the device efficiency despite the greater temperature gradient. As such, practical modules will utilize cold side temperatures ~400 K. To arrive at a representative number for $ZT_{avg}$, we separately prepared and measured the thermoelectric properties of five samples with the optimal doping composition $Na_{1.10}Pb_{10}Sb_{0.90}Se_{12}$ (data shown in Figure S10) and calculated the $ZT_{avg}$ for each. The value shown in Figure 8 of the main text ($ZT_{dev}$ ~ 0.64) is the average of the five samples.

## Additional data:

**Table S2.** Measured densities and fraction of the theoretical density (obtained by refinement of the powder XRD patterns) of $NaPb_mSbSe_{m+2}$, $Na_{1+x}Pb_{10-x}SbSe_{12}$, and $Na_{1+x}Pb_{10}Sb_{1-x}Se_{12}$. The densities were measured from the masses and volumes of the ~6x6x2 $mm^2$ squares used for the LFA measurements.

| Compound | Density ($g \cdot cm^{-3}$) | % of theoretical |
|---|---|---|
| $NaPb_{30}SbSe_{32}$ | 7.831 | 97 |
| $NaPb_{18}SbSe_{20}$ | 7.675 | 97 |
| $NaPb_{14}SbSe_{16}$ | 7.715 | 98 |
| $NaPb_{10}SbSe_{12}$ | 7.525 | 98 |
| $NaPb_8SbSe_{10}$ | 7.33 | 96 |
| $NaPb_4SbSe_6$ | 7.056 | 98 |
| $NaPb_2SbSe_4$ | 6.321 | 96 |
| $Na_{1.01}Pb_{9.99}SbSe_{12}$ | 7.292 | 95 |
| $Na_{1.03}Pb_{9.97}SbSe_{12}$ | 7.32 | 95 |
| $Na_{1.05}Pb_{9.95}SbSe_{12}$ | 7.35 | 95 |
| $Na_{1.10}Pb_{9.90}SbSe_{12}$ | 7.446 | 97 |
| $Na_{1.15}Pb_{9.85}SbSe_{12}$ | 7.469 | 97 |
| $Na_{1.20}Pb_{9.80}SbSe_{12}$ | 7.291 | 95 |
| $Na_{1.05}Pb_{10}Sb_{0.95}Se_{12}$ | 7.502 | 97 |
| $Na_{1.10}Pb_{10}Sb_{0.90}Se_{12}$ | 7.348 | 95 |
| $Na_{1.15}Pb_{10}Sb_{0.85}Se_{12}$ | 7.254 | 94 |

**Table S3.** Room temperature Hall coefficients and Hall carrier densities for $Na_{1+x}Pb_{10-x}SbSe_{12}$ and $Na_{1.10}Pb_{10}Sb_{0.90}Se_{12}$.

| Compound | $R_H$ ($cm^3 \cdot C^{-1}$) | $n_H$ ($10^{19} cm^{-3}$) |
|---|---|---|
| $Na_{1.01}Pb_{9.99}SbSe_{12}$ | 14.494 | 0.043 |
| $Na_{1.03}Pb_{9.97}SbSe_{12}$ | 0.284 | 2.198 |
| $Na_{1.05}Pb_{9.95}SbSe_{12}$ | 0.097 | 6.433 |
| $Na_{1.10}Pb_{9.90}SbSe_{12}$ | 0.062 | 10.028 |
| $Na_{1.15}Pb_{9.85}SbSe_{12}$ | 0.044 | 14.239 |
| $Na_{1.10}Pb_{10}Sb_{0.90}Se_{12}$ | 0.032 | 19.681 |

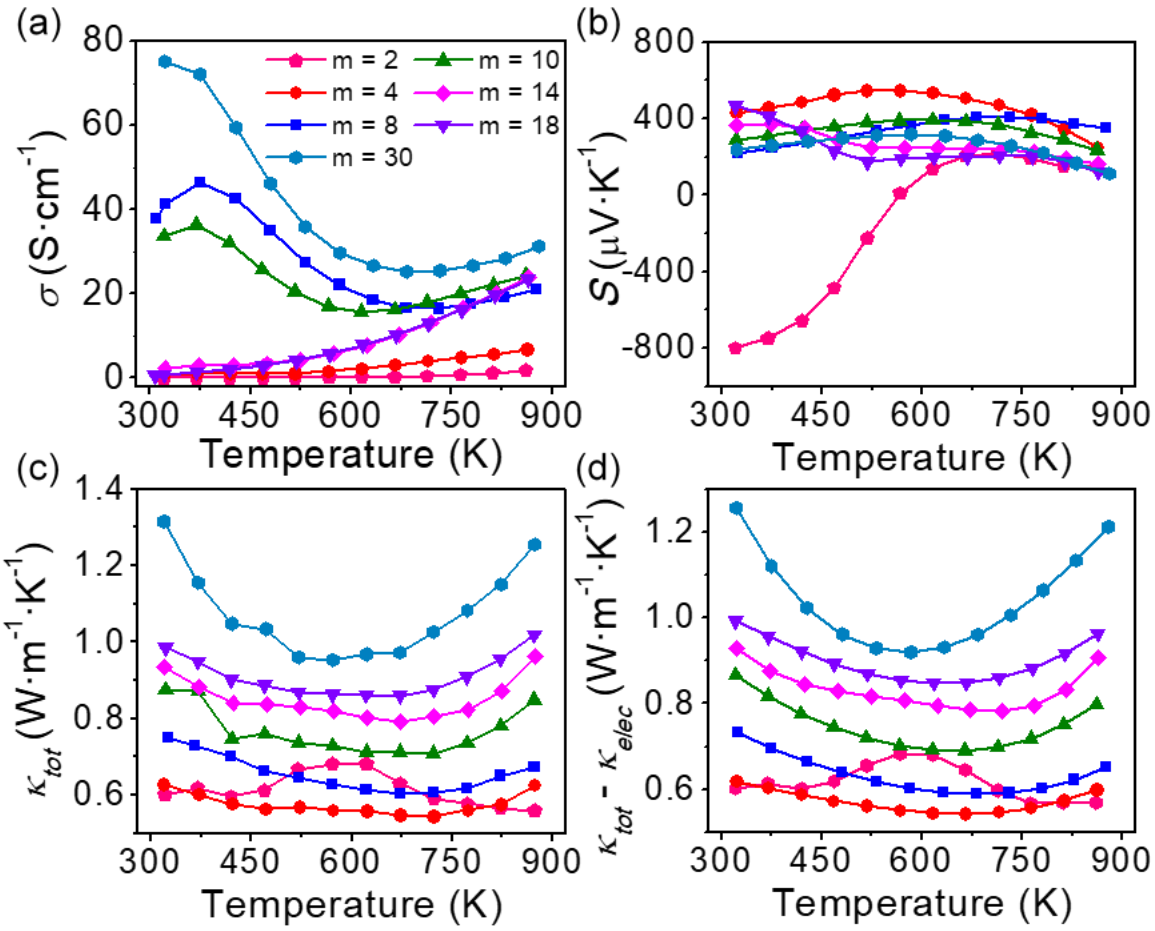


**Figure S2.** Temperature-dependent thermoelectric properties of nominally undoped of $NaPb_mSbSe_{m+2}$ (m = 2–30). (a) electrical conductivity, (b) Seebeck coefficients, (c) total thermal conductivity, and (d) estimated lattice thermal conductivity ($\kappa_{tot} - \kappa_{elec}$). The m = 8, 10, and 30 samples have slightly higher p-type electrical conductivities, potentially arising from cation vacancies or slight off-stoichiometry during the synthesis; the other compounds behave as undoped semiconductors as expected. All compounds show strong bipolar diffusion above 600 K as evident in the Seebeck coefficients and thermal conductivities, consistent with low charge carrier densities.

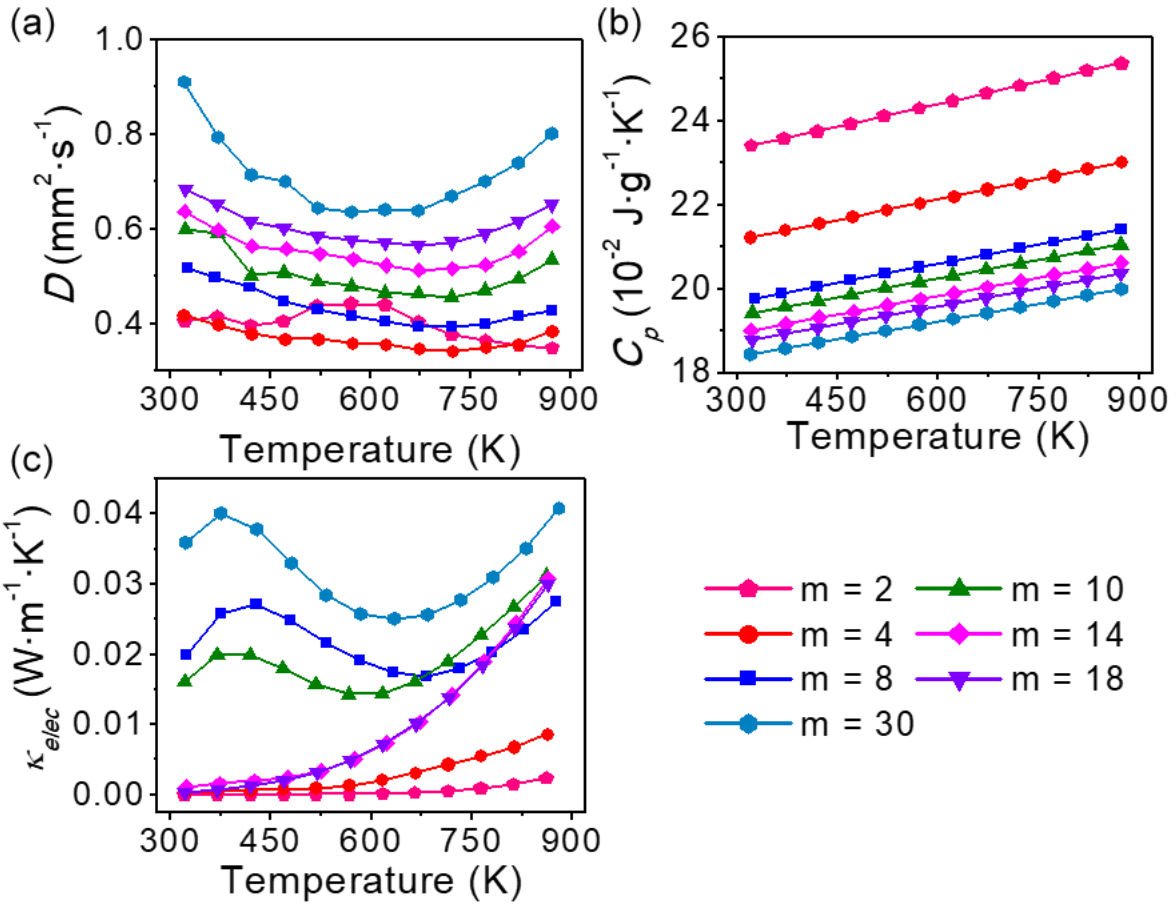


**Figure S3.** Temperature-dependent (a) thermal diffusivities, (b) estimated specific heats, (c) and calculated electronic thermal conductivities of nominally undoped $Na_{1+x}Pb_{10-x}SbSe_{12}$ (m = 2–30). For all samples shown above we used $L = 1.485 \times 10^{-8}$ $V^2 \cdot K^{-2}$.

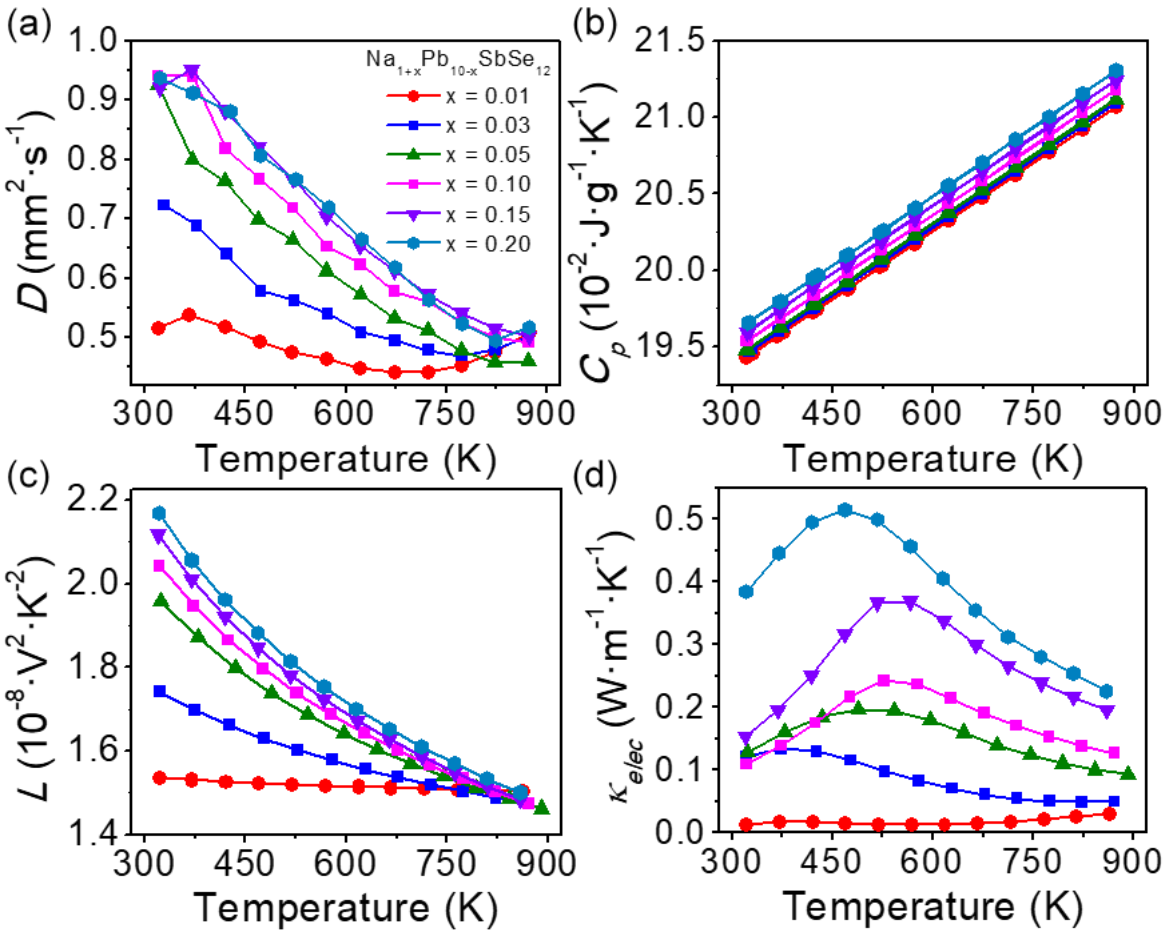


**Figure S4.** Temperature-dependent (a) thermal diffusivities, (b) estimated specific heats, (c) Lorentz numbers, and (d) calculated electronic thermal conductivities of $Na_{1+x}Pb_{10-x}SbSe_{12}$.

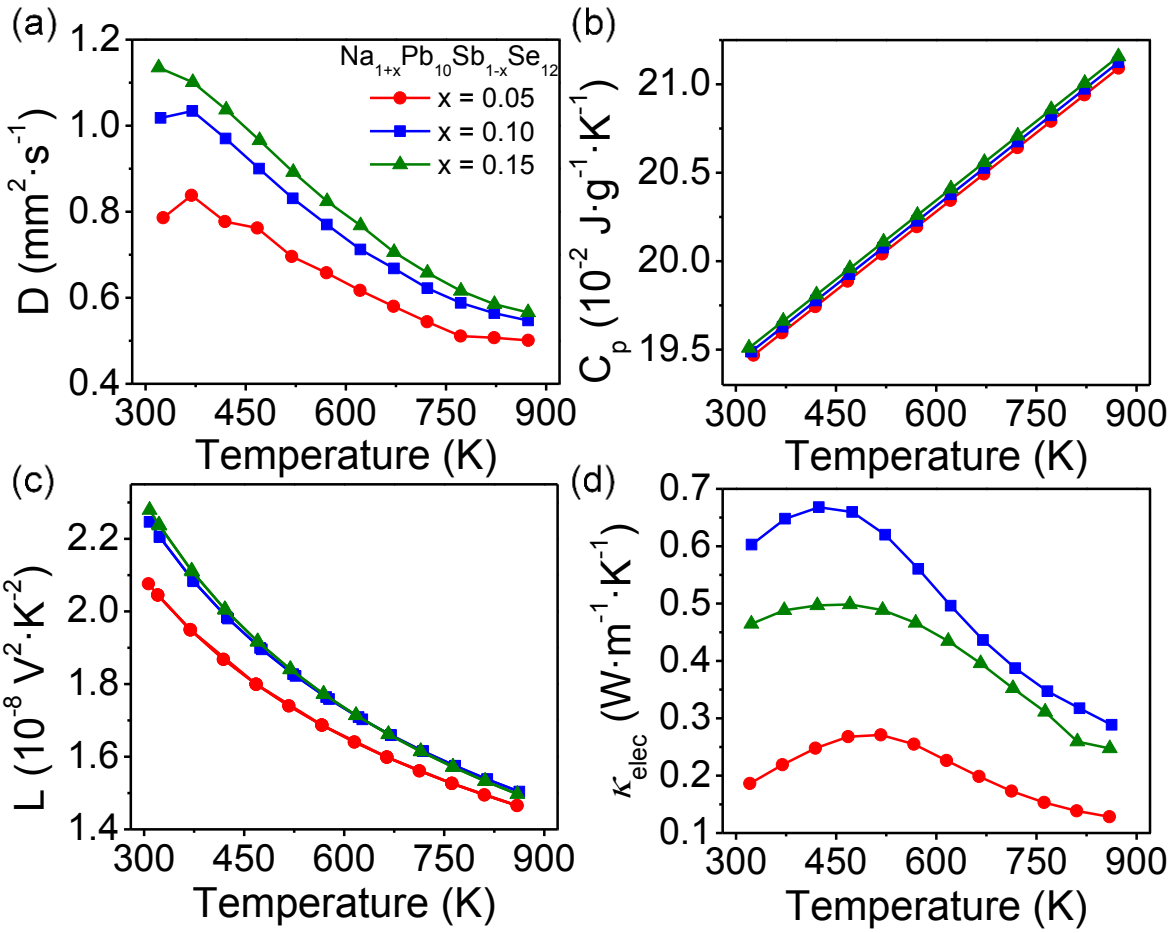


**Figure S5.** Temperature-dependent (a) thermal diffusivities, (b) estimated specific heats, (c) Lorentz numbers, and (d) calculated electronic thermal conductivities of $Na_{1+x}Pb_{10}Sb_{1-x}Se_{12}$.

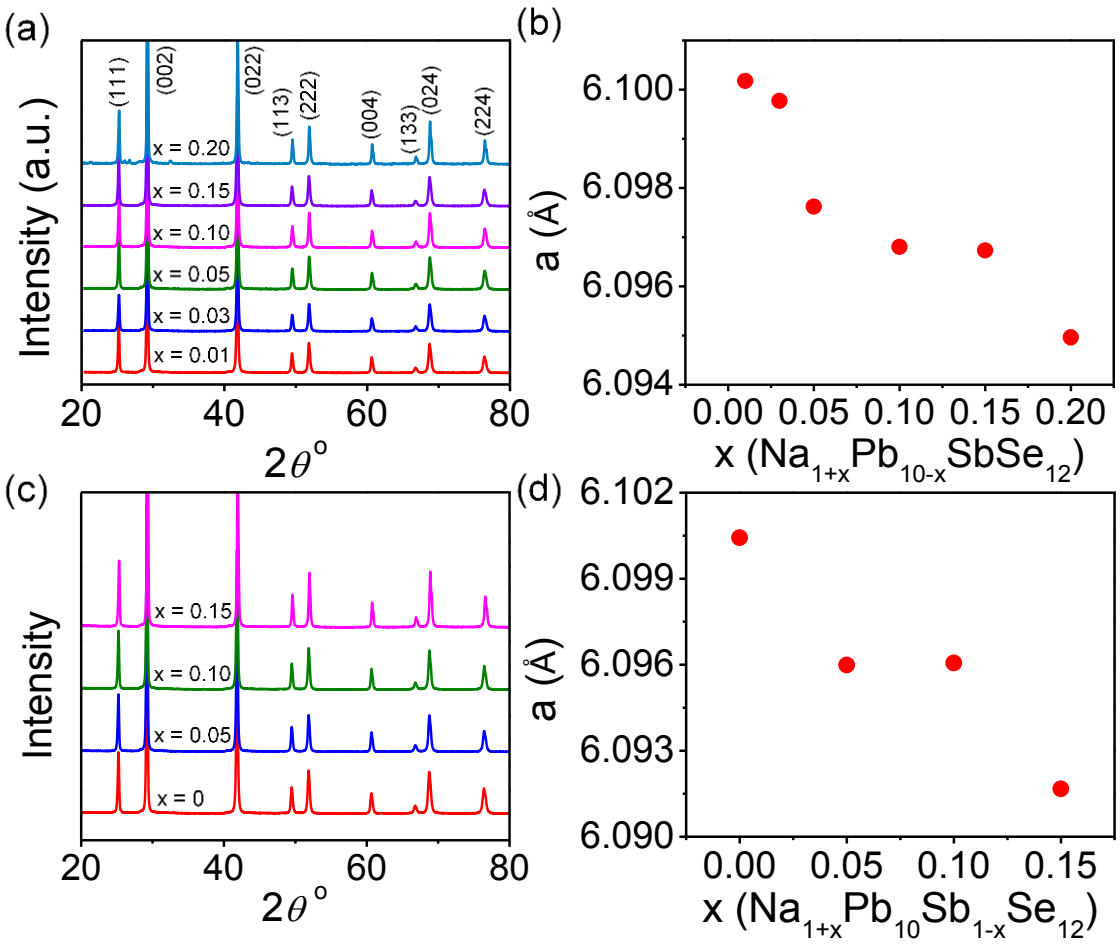


**Figure S6.** Powder X-ray diffraction patterns for $Na_{1+x}Pb_{10-x}SbSe_{12}$ (a) and $Na_{1+x}Pb_{10}Sb_{1-x}Se_{12}$ (c). (b) and (d) are respectively the refined lattice parameters for each. A small amount of secondary phases begin to be observed in (a) for x = 0.20.

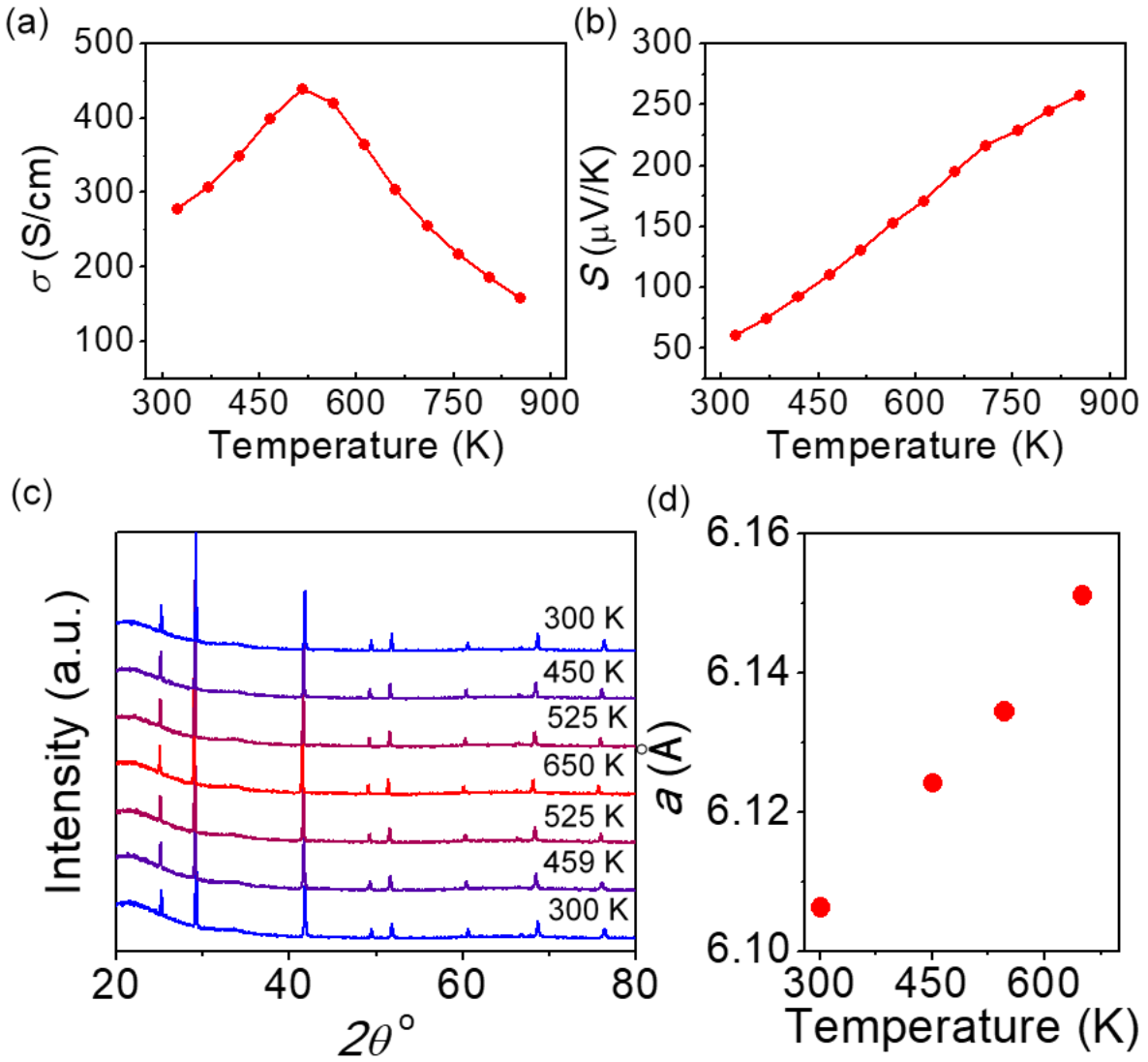


**Figure S7.** Temperature-dependent (a) electrical conductivity, (b) Seebeck coefficient, (c) variable-temperature powder X-ray diffraction patterns of a p-type $NaPb_mSbSe_{m+2}$ sample with nominal composition $Na_{1.10}Pb_{9.90}Sb_{0.90}Se_{12}$, and (d) refined lattice parameters from first four patterns shown in (c). The PXRD patterns show no clear changes upon heating and cooling, and the lattice parameters increase nearly linearly with heating as expected. These results suggest the unorthodox semiconducting-like electrical conductivity observed below 500 K and turnover to metallic charge transport above in (a) is not from a change in phase or change in dopant solubility.

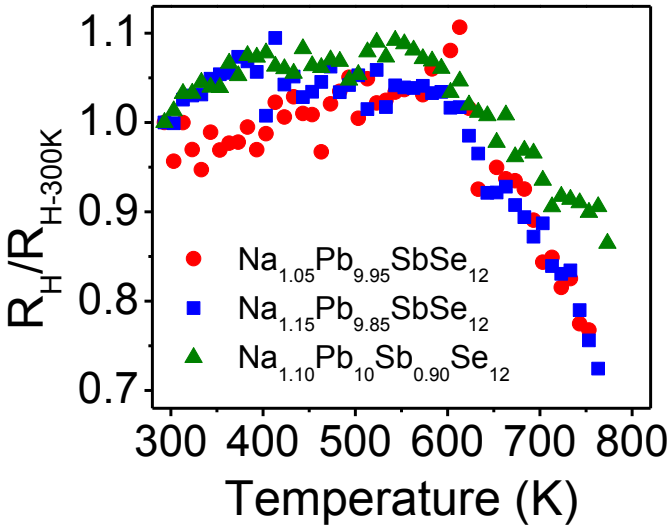


**Figure S8.** Hall coefficients for $Na_{1+x}Pb_{10-x}SbSe_{12}$ (x = 0.05, 0.15) and $Na_{1.10}Pb_{10}Sb_{0.90}Se_{12}$ (normalized by respective values of $R_H$ at 300 K) showing that $R_H$ increases weakly with temperature between 300 and ~550K. The onset of the decrease in $R_H$ shifts slightly towards lower temperature as the carrier density increases, consistent with the Fermi level moving closer to the $\Sigma$-band and inconsistent with bipolar diffusion.

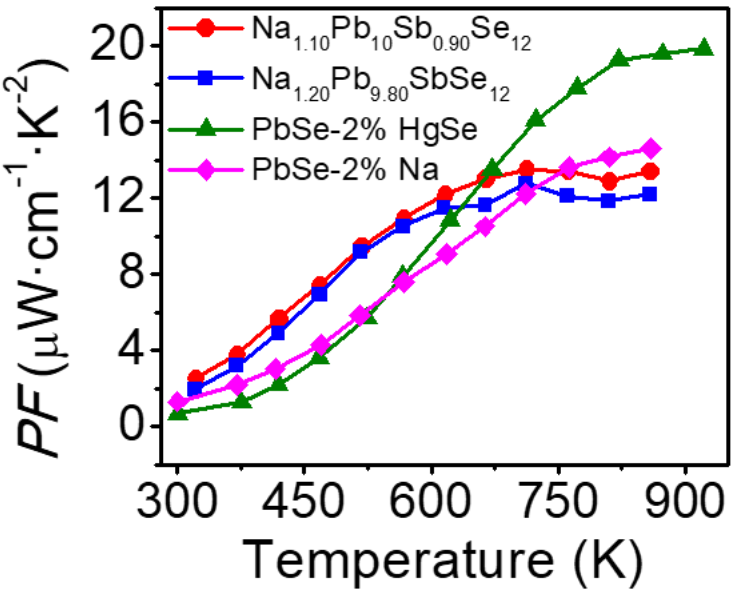


**Figure S9.** Temperature-dependent power factors of two differently doped $NaPb_{10}SbSe_{12}$ samples compared with those of PbSe-2%Na and band engineered PbSe-2% HgSe (2% Na doped).[10] The PbSe-HgSe exhibits a record high power factor ~20 $\mu W \cdot cm^{-1} \cdot K^{-2}$ above 900 K; however, the $NaPb_{10}SbSe_{12}$ have superior power factors below ~ 700 K that contribute to outstanding average *ZT*s discussed in the main text. Considering each of the compounds shown above has comparable carrier densities ~$2x10^{20}$ $cm^{-3}$, we attribute the high power factors below 700 K in $NaPb_{10}SbSe_{12}$ to the greater contribution of the $\Sigma$-band. Namely, as discussed in the main text, in $NaPb_{10}SbSe_{12}$ both *L*- and $\Sigma$-bands participate in the charge transport even near room temperature, which should improve the power factors at low and moderate temperatures due to the high valley degeneracy.

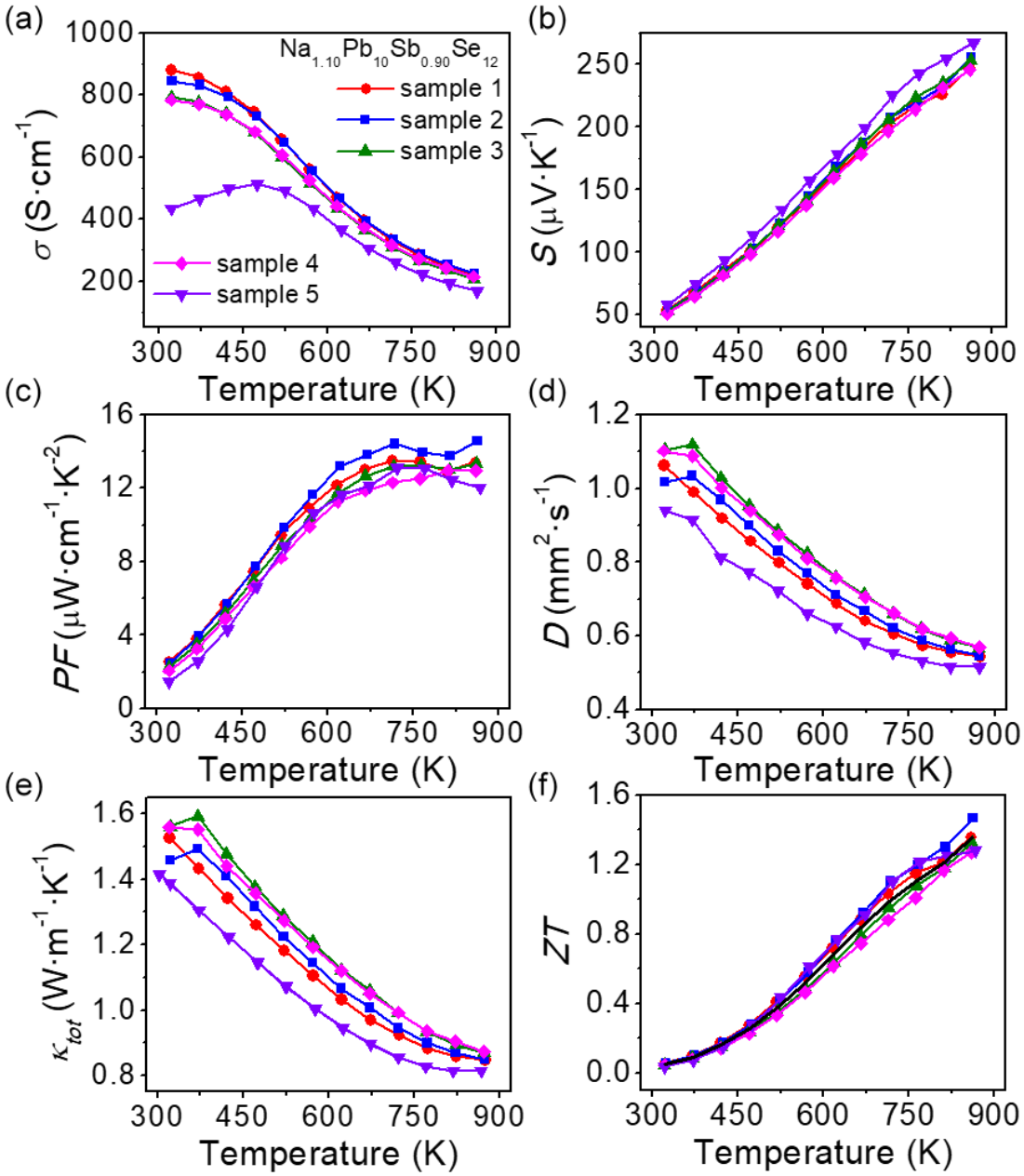


**Figure S10.** Temperature dependent thermoelectric properties of five separately prepared samples of the optimally doped $Na_{1.10}Pb_{10}Sb_{0.90}Se_{12}$. (a) electrical conductivities, (b) Seebeck coefficients, (c) powerfactors, (d) thermal diffusivities, (e) total thermal conductivities, and (f) *ZT*s. The solid black line in (f) traces the average values of the temperature dependent *ZT* curves calculated at each temperature and is used in the comparison with the literature found in Figure 8 of the main text. Sample 5 likely has a lower carrier concentration, evidenced by the lower $\sigma$ and higher *S*. The measurements are consistent above ~500 K but show more variability below. This is likely because the grain boundary carrier scattering may be very sensitive to the precise conditions at the GBs, which likely differs slightly from sample to sample. The measurements show good reproducibility within the 15% uncertainty typical of thermoelectric measurements.

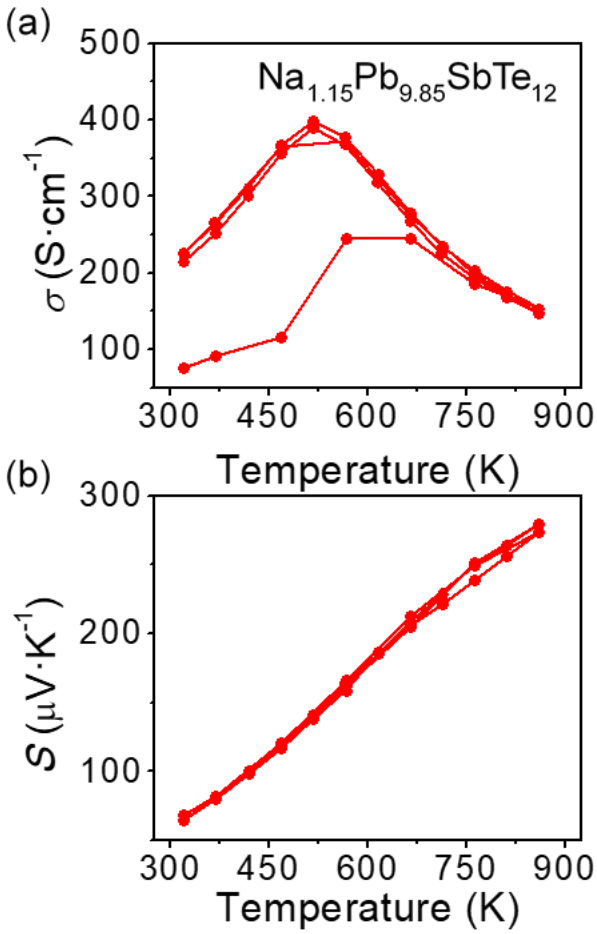


**Figure S11.** Temperature dependent (a) electrical conductivities and (b) Seebeck coefficients for a sample with nominal composition $Na_{1.15}Pb_{9.85}SbSe_{12}$. Two full heating and cooling cycles between 323 and 873 K are displayed, and the electrical conductivity clearly shows significant hysteresis between the first heating and cooling profile. The properties stabilize upon cooling and show little hysteresis upon further heating and cooling cycles. The Seebeck coefficients have negligible hysteresis, indicating the changes shown in (a) may originate at the grain boundaries. We measured a heating and cooling profile on all samples considered in this work, all of which show hysteresis in the electrical conductivity between the first heating and cooling profile like what is shown above. Because the properties generally stabilize on cooling and further heating, all thermoelectric data reported in this work comes from the cooling profile, as discussed in the experimental section of the main text.

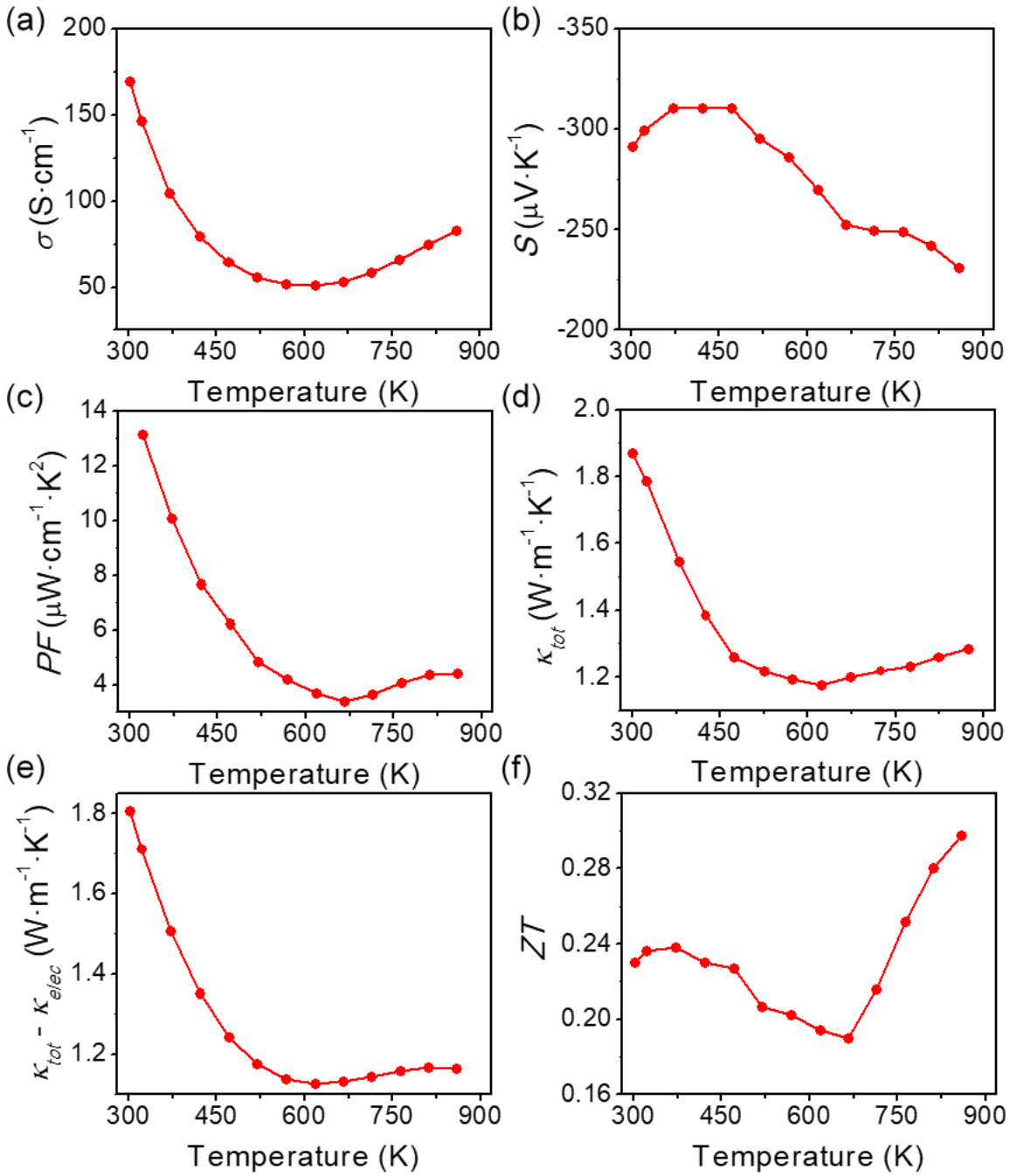


**Figure S12.** Temperature-dependent thermoelectric properties of a pure (nominally undoped) PbSe sample included for comparison with our PbSe-$NaSbSe_2$ alloys. (a) electrical conductivities, (b) Seebeck coefficients, (c) power factors, (d) total thermal conductivities, (e) estimated lattice thermal conductivities, and (f) *ZT*s.

## References:


[1] I. U. I. Ravich, B. A. Efimova, I. A. Smirnov, *Semiconducting lead chalcogenides*, Plenum Press, New York, **1970**.

[2] A. F. May, E. S. Toberer, A. Saramat, G. J. Snyder, *Physical Review B* **2009**, *80*, 125205.

[3] Y. Pei, A. D. LaLonde, H. Wang, G. J. Snyder, *Energy & Environmental Science* **2012**, *5*, 7963-7969.

[4] H. Wang, Y. Pei, A. D. LaLonde, G. J. Snyder, *Proceedings of the National Academy of Sciences* **2012**, *109*, 9705-9709.

[5] T. C. Chasapis, Y. Lee, E. Hatzikraniotis, K. M. Paraskevopoulos, H. Chi, C. Uher, M. G. Kanatzidis, *Physical Review B* **2015**, *91*, 085207.

[6] J. Callaway, *Physical Review* **1959**, *113*, 1046-1051.

[7] J. He, L.-D. Zhao, J.-C. Zheng, J. W. Doak, H. Wu, H.-Q. Wang, Y. Lee, C. Wolverton, M. G. Kanatzidis, V. P. Dravid, *J. Am. Chem. Soc.* **2013**, *135*, 4624-4627.

[8] L. Fu, M. Yin, D. Wu, W. Li, D. Feng, L. Huang, J. He, *Energy & Environmental Science* **2017**, *10*, 2030-2040.

[9] G. J. Snyder, A. H. Snyder, *Energy & Environmental Science* **2017**, *10*, 2280-2283.

[10] J. M. Hodges, S. Hao, J. A. Grovogui, X. Zhang, T. P. Bailey, X. Li, Z. Gan, Y.-Y. Hu, C. Uher, V. P. Dravid, C. Wolverton, M. G. Kanatzidis, *J. Am. Chem. Soc.* **2018**.